Alkali Ions Pre-Intercalated Layered MnO 2 Nanosheet for Zinc-Ions Storage

Liyuan Liu, Yih-Chyng Wu, Liang Huang, Kaisi Liu, Benjamin P Duployer, Patrick Rozier, P.-L. Taberna, Patrice Simon

Wiley Analytical Science

Wiley Analytical Science Virtual Conference

November 9-17

For the 3rd time, The Wiley Analytical Science Conference is back!

It's all happening November 9 - 17

The Wiley Analytical Science Virtual Conference will bring together thousands of researchers and practitioners to share current developments in science and industry. Join for exciting presentations from experts in the fields of analytical and bioanalytical chemistry, pharmaceutical research, materials science, lab automation, and related disciplines.

Register to learn about recent developments & applications in:

- Microscopy
- Spectroscopy
- Mass Spectrometry
- Separation Science
- Much more!

Register here

WILEY

ADVANCED ENERGY MATERIALS
www.advenergymat.de

Alkali Ions Pre-Intercalated Layered MnO_2 Nanosheet for Zinc-Ions Storage

*Liyuan Liu, Yih-Chyng Wu, Liang Huang, Kaisi Liu, Benjamin Duployer, Patrick Rozier, Pierre-Louis Taberna, and Patrice Simon**

Recently, rechargeable zinc-ion batteries in mild acidic electrolytes have attracted considerable research interest as a result of their high sustainability, safety, and low cost. However, the use of conventional Zn-ion storage materials is hindered by insufficient specific capacity, sluggish reaction kinetics, or poor cycle life. Here, these limitations are addressed by pre-intercalating alkali ions and water crystals into layered δ-MnO_2 (birnessite) to prepare $K_{0.27}MnO_2{\cdot}0.54H_2O$ (KMO) and $Na_{0.55}Mn_2O_4{\cdot}1.5H_2O$ with ultrathin nanosheet morphology via a rapid molten salt method. In these materials, alkali ions and water crystals act as pillars to stabilize the layered structures, which can enable rapid diffusion of cations in the KMO structure, resulting in high power capability (90 mAh g^{-1} at 10 C) and good cycling stability. Furthermore, electrochemical quartz crystal microbalance measurements shed light on the charge storage mechanism of KMO in an aqueous Zn-ion battery which, combined together with in-operando X-ray diffraction techniques, suggests that the charge storage process is dominated by the (de)intercalation of H_3O^+ with further dissolution–precipitation of $Zn_4(OH)_6(SO_4){\cdot}5H_2O$ solid product on the KMO surface during cycling.

1. Introduction

Compared with organic electrolytes, aqueous electrolytes are safer (no risk of burning) and can achieve an ionic conductivity several orders of magnitude higher than organic electrolytes.[1–4] This makes aqueous rechargeable batteries cheap, non-polluting and safe, with potentially high power density capability (although the cell voltage is limited).[1] However, the widely studied aqueous lithium-ion batteries and sodium-ion batteries have low specific capacities (<150 mAh g^{-1}).[2] Among potential alternatives, the aqueous Zn-ion battery (AZIB) is currently attracting significant attention due to key features of Zn metal, including abundance (low cost) and high theoretical specific capacity (820 mAh g^{-1}).[5–9] The main challenges for the development of aqueous Zn-ion batteries are to achieve dendrite-free Zn deposit at the anode[10,11] and find suitable cathode materials. MnO_2 (theoretical capacity is 308 mAh g^{-1}) is one of the most attractive cathode materials for aqueous zinc ion batteries due to their high energy density and high power density.[5,6,8,11–15] Among various crystallographic polymorphs (α-, β-, γ-, δ-, λ-, and ε-type), birnessite-type δ-MnO_2 with layered structure owns a large interlayer spacing (≈0.7 nm), which is more suitable for rapid and reversible (de-)insertion of Zn ions.[16] However, δ-MnO_2 was reported to show poor rate capability and cycling stability.[15] According to the literature, δ-MnO_2-based cathodes are limited by the serious structural degradation with phase transformation, which is mainly attributed to the co-intercalation of water molecules and dissolution of Mn during cycling processes.[17,18] It has been reported that the pre-intercalation of large cations (such as, K^+, Ce^{3+}, and Ca^{2+}) in MnO_2 during synthetic process can stabilize the structure through coordination of guest-ions with adjacent host atoms.[16,19–25] Moreover, the preintercalation of alkaline ion strategy in MnO_2 has also attracted much attention as an effective approach to enhance the electronic conductivity, activating more active sites, and promoting diffusion kinetics.[25]

To date, various types of reaction mechanisms have been reported for Mn oxide-based positive electrode of Zn-MnO_2 battery in Zn-containing aqueous electrolyte.[15,26–28] Pan et al.[26] proposed a chemical-assisted conversion reaction mechanism

Dr. L. Liu, Dr. Y.-C. Wu, B. Duployer, Prof. P. Rozier, Dr. P.-L. Taberna, Prof. P. Simon
CIRIMAT
UMR CNRS 5085
Université Paul Sabatier Toulouse III
118 route de Narbonne, Toulouse 31062, France
E-mail: simon@chimie.ups-tlse.fr
Dr. L. Liu, Dr. Y.-C. Wu, B. Duployer, Prof. P. Rozier, Dr. P.-L. Taberna, Prof. P. Simon
RS2E
Réseau Français sur le Stockage Electrochimique de l'Energie
FR CNRS 3459, Amiens Cedex 80039, France
Prof. L. Huang, K.-S. Liu
Wuhan National Laboratory for Optoelectronics
Huazhong University of Science and Technology
Wuhan, Hubei 430074, China

The ORCID identification number(s) for the author(s) of this article can be found under https://doi.org/10.1002/aenm.202101287.

DOI: 10.1002/aenm.202101287

between α-MnO_2 and MnOOH from TEM observation and NMR spectroscopy measurements. MnOOH was formed likely by intercalation of H^+ from H_2O in MnO_2, while the resulting OH^- ions further react with $ZnSO_4$ thus forming $ZnSO_4[Zn(OH)_2]_3 \cdot xH_2O$ at the surface of the electrode.[26] Another mechanism based on Zn^{2+} insertion/extraction from MnO_2 was proposed by Alfaruqi et al., who observed the formation of $ZnMn_2O_4$ and Zn_xMnO_2, via ex situ X-ray diffraction (XRD) analysis.[15] Moreover, Sun et al. reported the co-insertion of H^+ and Zn^{2+} by galvanostatic intermittent titration technique and ex situ XRD analysis,[27] where Zn^{2+} intercalation occurred only after H^+ insertion during the reduction process. However, ex situ XRD analysis may introduce some uncertainty because of the need for cell dismantling. Finally, Guo et al. recently proposed a charge storage mechanism at the positive MnO_2 electrode in the mild acidic electrolyte, dominated by a dissolution–precipitation of $ZnSO_4[Zn(OH)_2]_3 \cdot xH_2O$. At the same time, they propose that only a minor capacity contribution was coming from the (de)intercalation of H^+ and Zn^{2+}, which may be questionable since the $Zn_4(OH)_6(SO_4) \cdot 5H_2O$ (ZHS) precipitation is a chemical mechanism.[28]

In this work, we study the electrochemical behavior of MnO_2 electrode pre-intercalated with alkali ions (Na-ion or K-ion), which expands the MnO_2 interlayer distance for fast ion diffusion, while consolidating (pillar effect) the expanded layer structure at the same time. Furthermore, a series of advanced techniques including in-operando XRD and electrochemical quartz crystal microbalance (EQCM) have been used to understand the charge storage mechanism. While the precipitation of ZHS on the surface of the electrode makes it difficult to distinguish between Zn^{2+} or H_3O^+ intercalation by in-operando XRD technique, EQCM experiments shed light on the charge storage mechanism of $K_{0.27}MnO_2 \cdot 0.54H_2O$ (KMO) in AZIBs.

2. Results and Discussion

2.1. Materials Characterizations

Low-temperature molten salt mixtures were prepared using low melting inorganic salts such as nitrates, sulfates or chlorides.[26] Since salt is at a molten state, ions have a higher diffusion coefficient (10^{-5} to 10^{-8} cm^2 s^{-1})[27] and diffuse faster than the conventional solid-state chemistry route (diffusion coefficient is in the order of 10^{-18} cm^2 s^{-1}),[27] resulting in an enhancement of the reaction kinetics and homogeneous mixing of reactants.[27–29] In our experiments, nitrate powder was firstly heated in air to reach a molten state (**Figure 1**a). The precursor powder ($MnSO_4$) was then added to the melt and the reaction time was kept to only 1 min, leading to the formation of solid product well dispersed in the colorless molten salt (Figure 1b). Once cooled down to room temperature (air quench), the recrystallized salt was solubilized in water and the KMO was recovered by filtration (Figure 1c). More synthesis details have been given in the experimental part.

After removing the extra salts, the structure, composition and morphology of the samples were analyzed by XRD, SEM, and TEM. The XRD pattern in **Figure 2**a displays mainly four characteristic peaks at 12.5°, 25.0°, 36.7°, 65.9°, which are indexed with respectively (003), (006), (012), and (110) planes of KMO (JCPDS 52-0556). The rhombohedral structure of KMO (a = 2.849 Å, b = 2.849 Å, and c = 21.536 Å) is built from layers of edge-shared [MnO_6] octahedra stacked along [001] with K^+ and H_2O intercalated in interlayer space, as shown in the inset of Figure 2a. The diffraction peaks are broad, suggesting nano-sized crystallites roughly estimated around 5 nm using Scherrer's equation.[30] SEM (Figure S1, Supporting Information) and TEM (Figure 2b) experiments images reveal that KMO adopts a 2D nanosheet morphology which is expected to be favorable for cation (Zn^{2+} and/or H^+) insertion/extraction. As shown in Figure 2c, sample thickness was measured to about 3.2 nm, corresponding to ≈4 layers considering the thickness of a monolayer (7.18 Å). Atomic force microscopy (AFM) image even shows a smaller thickness of about 2–3 nm (see Figure S2a, Supporting Information). This supports the formation of ultrathin 2D KMO morphology. Moreover, a BET surface area of 123.74 m^2g^{-1} was measured (see Figure S2b, Supporting Information), resulting in improved accessible surface area for redox activity. EDS elemental mapping images depicted in Figure S3, Supporting Information, show that K, Mn, and O are homogeneously distributed in the KMO.

Furthermore, the surface composition was checked by X-ray photoelectron spectroscopy (XPS), as shown in Figure 2d–f. The Mn2p signal is split into two contributions corresponding to the presence of Mn^{3+} and Mn^{4+} chemically bound with oxygen, while the O1s energy level can be split into three peaks, corresponding to Mn—O—Mn, Mn—O—H, and H—O—H contributions.[28] This result confirms that the interlayer water molecules form chemical bonds with the MnO_2 layers, indicating a good structure stability of KMO structure. Na-intercalated MnO_2 was also prepared from the same synthesis method. Monoclinic

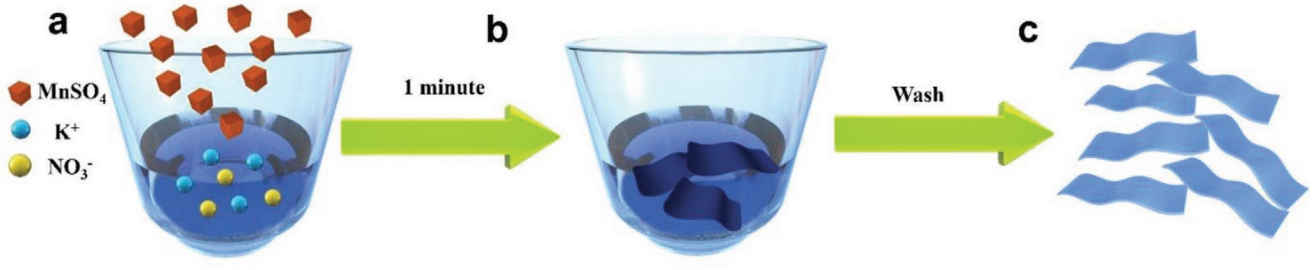

Figure 1. Schematic representation of molten salt method synthesis process. a) The $MnSO_4$ powder precursor was added into the molten KNO_3. b) The sample was removed from the furnace after 1 min. c) The samples were obtained after washing with deionized water.

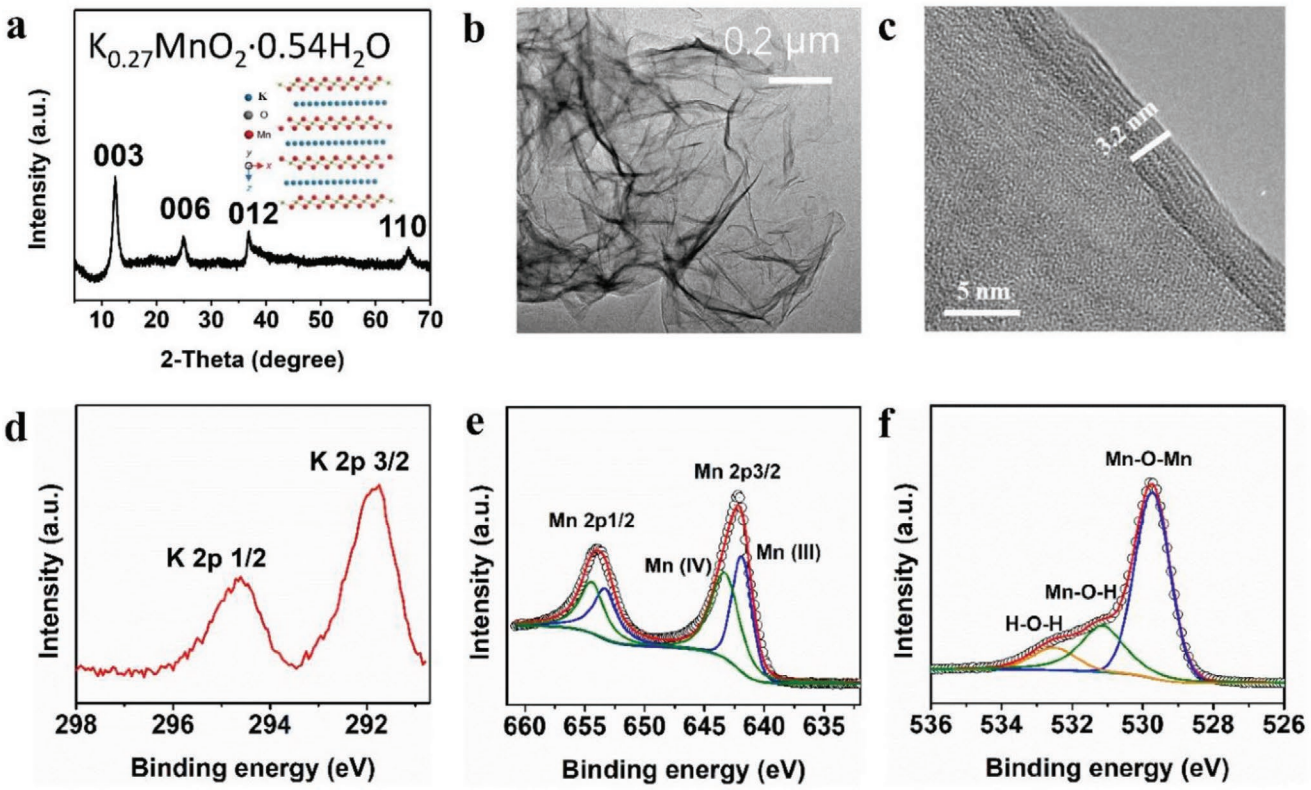

Figure 2. Characterization of $K_{0.27}MnO_2 \cdot 0.54H_2O$. a) XRD pattern and structure, b) low resolution TEM images, c) high resolution TEM images, XPS spectrums of d) K 2p, e) Mn 2p, and f) O1s.

$Na_{0.55}Mn_2O_4 \cdot 1.5H_2O$ (NMO) (JCPDS 43-1456) was identified using the X-ray diffraction technique, with Na-ion and crystal water filling the interlayer gap, with a similar 2D nanosheet morphology (Figures S4 and S5, Supporting Information).

2.2. Electrochemical Characterizations

Figure 3a shows the initial three charge/discharge galvanostatic plots test at C/3 (1 C = 0.3 Ag^{-1}) current rate within a potential window of 0.7–1.8 V versus Zn^{2+}/Zn. The initial discharge profile shows a clear plateau located at 1.25 versus Zn^{2+}/Zn with an open-circuit voltage of about 1.45 V versus Zn^{2+}/Zn; another small discharge plateau is also visible at 1.38 V versus Zn^{2+}/Zn. During subsequent discharges, two plateaus with similar capacity are observed. During charge, mainly one single plateau is observed at 1.52 V versus Zn^{2+}/Zn although a slight potential increase can be seen at about 150 mAh.g^{-1}, which could correspond to the transition between the two redox plateaus observed on discharge. This electrochemical profile is similar to the ones reported for MnO_2 used as cathode in aqueous ZIBs.[31] The initial discharge and charge capacity are around 288 mAh g^{-1}, which is close to the theoretical capacity (308 mAh g^{-1}, based on the molecular weight of MnO_2 and 1 e^- transfer reaction).[32] Figure 3b shows the galvanostatic profiles from C/3 to 10 C-rate. The maximum discharge capacity of 280 mAh g^{-1} achieved at C/3 decreases of about 14% (240 mAh g^{-1}) at 1 C. Interestingly, 90 mAh g^{-1} could still be delivered at 10 C, indicating the high-power capability of the KMO electrode. These values positively compare with MnO_2 with nanorod morphology,[33] and it is also competitive compared with other MnO_2 with 2D nanosheet structure.[15,24,34] This could be ascribed to the ultrathin nanosheet morphology of KMO, which increased surface area contact between the electrolyte and active material and reduce the diffusion distance.[35] Figure 3c shows the voltage profile and the discharge capacity at C/3. The capacity decreases during the first 20 cycles and remains then stable at about 260 mAh.g^{-1}. As a whole, the capacity retention reaches 86% after 100 cycles with a minimal loss of 3% between the 20th and 100th cycles (Figure 3d). When the current density increases to 5 C, the capacity retention reaches 92% after 300 cycles (Figure S6, Supporting Information). Moreover, as shown in Figure 3e, the cycling stability of KMO was also evaluated at a high current density (10 C). A decent specific capacity of 84 mAh g^{-1} was measured after 1000 cycles; as a result of the fast charge/discharge rate, the capacity retention was improved to reach 91% at the 1000th cycle. This cycling stability compare positively to most of the reported δ-MnO_2 materials for Zn-ion batteries (see Table S1, Supporting Information),[19–21,23–25] and similar to the previously reported other ions pre-intercalated MnO_2 as cathode for Zn-ion batteries as shown in Table S2, Supporting Information.[9,11,17,18,24,33] The good cycling stability could be explained by the pre-intercalated K^+ and H_3O^+ in the KMO structure, as a result of charge balancing,[28] which acts as pillars to stabilize the layered structures.[29]

The high K-ion insertion capacity, rate capability and capacity retention reported for the present KMO in aqueous Zn-ion battery positively compares with most of the other previously

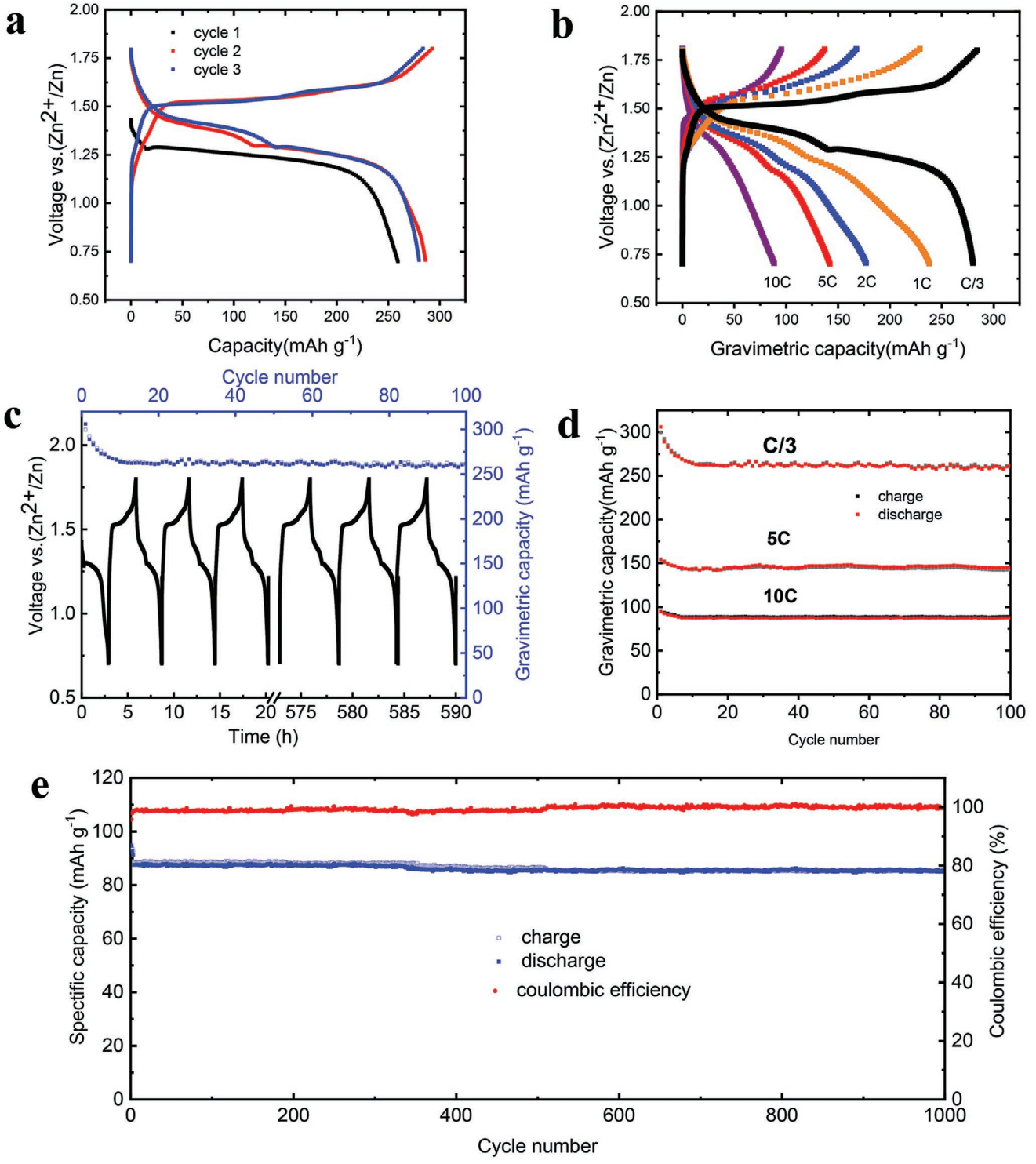

Figure 3. Electrochemical characterization of $K_{0.27}MnO_2{\cdot}0.54H_2O$ in 2 M $ZnSO_4$ + 0.3 M $MnSO_4$ electrolyte. a) Galvanostatic charge/discharge profiles of the first three cycles at C/3. b) Discharge–charge curves at various C-rates. Cycling performance at a current density of c) C/3 and e) 10C. d) Comparison of cycling stability of first 100 cycles at C/3, 5 C, and 10 C.

reported Zn-MnO_2 batteries[5,14,15,17,18,33,34,36–39] (see Table S1, Supporting Information). Additionally, the rapid and simple synthesis route and the limited synthesis temperature used to prepare our NMO (350 °C) and KMO (380 °C) makes the process and materials competitive versus all the MnO_2 used as cathode in Zn-ion batteries listed in Table S1, Supporting Information. However, beyond the electrochemical performance, a key point is the understanding of the charge storage mechanism in MnO_2 electrodes for zinc ion battery applications, and this will be the focus of the next part. Indeed, several

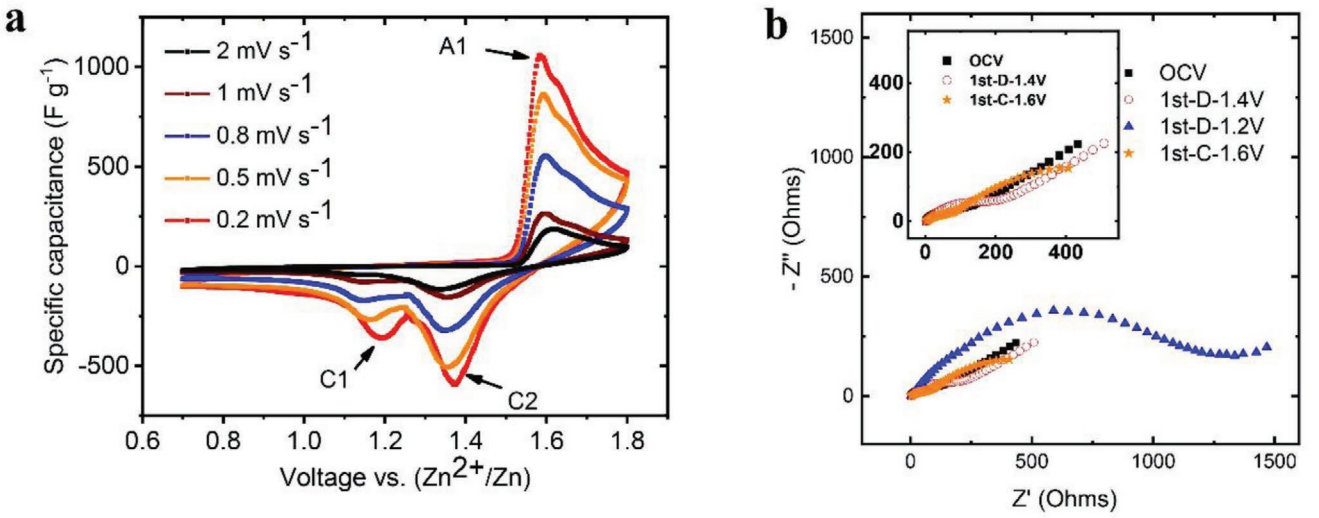

Figure 4. Characterizations of $K_{0.27}MnO_2{\cdot}0.54H_2O$ in 0.3 M $MnSO_4$ + 2 M $ZnSO_4$ aqueous electrolyte; a) CV curves recorded at various potential scan rates from 0.2 to 2 mV s^{-1}. b) EIS analysis at different potentials during the first cycle.

mechanisms were reported in the literature to describe the reaction mechanism of MnO_2-based electrode in $ZnSO_4$-based aqueous electrolyte, ranging from Zn^{2+} and/or H^+ cations intercalation to balance the reduction of M^{+IV} cations, to MnO_2 dissolution into Mn^{2+} followed by precipitation of zinc hydroxysulfate (ZHS) salt.[15,31,37,40]

2.3. Reaction Kinetics

Cyclic voltammetry tests were performed at various potential scan rates to gain insight into the reaction kinetics of KMO in ZIBs. **Figure 4**a shows CV plots of a KMO electrode recorded at different scan rates. At 0.2 mV s^{-1}, there is one main sharp obvious oxidation peak located at 1.59 V s. Zn^{2+}/Zn, associated with another slight peak at 1.62 V versus Zn^{2+}/Zn. During the reduction process, two peaks centered at 1.23 and 1.38 V versus Zn^{2+}/Zn are visible, in line with the potential plateaus observed during galvanostatic experiments (Figure 3a). These two redox peaks suggest at least two steps are involved in the reaction mechanism. According to the report of Kim et al.,[41] the reduction peak located at 1.38 V versus Zn^{2+}/Zn corresponds to the reduction of MnO_2 into MnOOH, while the other peak centered at 1.23 V versus Zn^{2+}/Zn could be associated with the further reduction of MnOOH into soluble Mn^{2+}. During oxidation, Mn^{2+} is converted back into MnO_2 via the reverse process. Such a mechanism was proposed based on ex situ XRD analyses.[41]

Moreover, according to the relationship between the peak current and scan rate as shown in the following Equation (1):[42]

$$i = av^b \tag{1}$$

where the b value can be calculated by plotting the peak current i (mA g^{-1}) versus the scan rate v (mV s^{-1}) in log scale (see Figure S7, Supporting Information), which is obtained from Figure 4a. The b value of the anodic peak was calculated at 0.61 while the other two cathodic peaks were 0.58 and 0.52, respectively. Since all these three b values are approaching 0.5, we can deduce that the Zn-ion charge storage process is mainly controlled by the ion diffusion in the KMO material.

Electrochemical impedance spectroscopy (EIS) measurements were also performed at different potentials during the discharge process of the KMO·electrode to have a further understanding of the reaction kinetics. As shown in Figure 4b, the large difference in different potential regions can be observed. The EIS plot at 1.4 V versus Zn^{2+}/Zn during discharge shows the expected signature, with a high frequency loop associated with a charge transfer resistance, followed by a 45° Warburg impedance characteristic of semi-infinite ion diffusion behavior.[43] However, when the discharge potential is decreased down to 1.2 V, a large loop is visible, resulting in a drastic impedance increase. This loop, which could be associated with a charge transfer process in a first approximation, evidences a major change in the electrode mechanism associated with a shift of the electrode impedance along the real part of the real axis (see later). When the potential is increased back to 1.6 V, the charge transfer resistance decreases back to the initial value (≈125 Ω) and the EIS signature stands for a semi-infinite diffusion behavior.[43] The sharp peak current during the oxidation at 1.59 V (see Figure 4a) in the CV curve also supports the diffusion limitation during the oxidation process.

To get further insights about the cation at the origin of the charge compensation during the reduction process (Zn^{2+} or/and H_3O^+), KMO electrode has also been tested in Zn^{2+}-free, 0.3 M $MnSO_4$ electrolyte and the result is shown in Figure S8, Supporting Information. In 0.3 M $MnSO_4$ electrolyte, a sloping discharge profile can be observed together with 41% capacity retention, which makes it difficult to assign to either Zn^{2+} or H^+ cations.

2.4. Charge Storage Mechanism

In situ XRD study (**Figure 5**) was performed (2θ range of 5° to 60°) to evaluate the structure and phase transformation of KMO during charge/discharge cycles. Under the operating conditions used for in situ experiments (low mass loading combined with

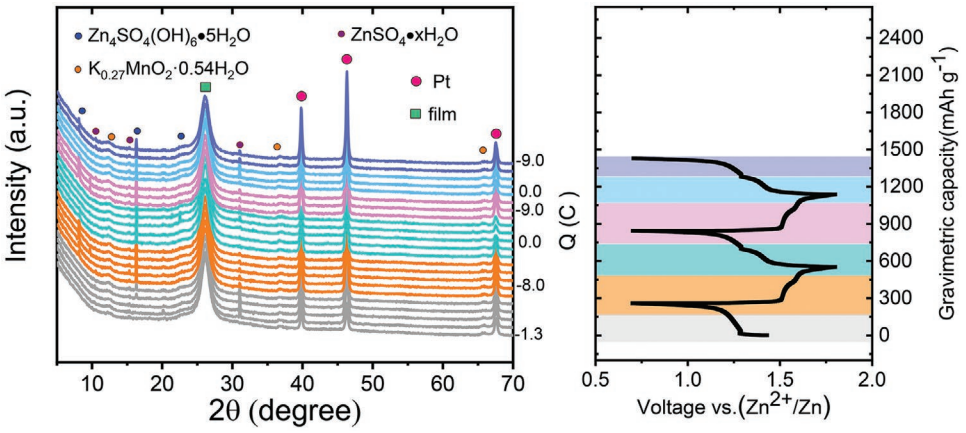

Figure 5. In situ XRD patterns of the $K_{0.27}MnO_2·0.54H_2O$ in 2 M $ZnSO_4$ + 0.3 M $MnSO_4$ electrolyte cell under a current rate of C/3, corresponding to the voltage-capacity curve given on the right.

fast XRD scan rate), it was not possible to detect KMO diffraction peaks, such as already reported for similar experiments with MnO_2 materials.[40] Besides, the diffraction peaks located, for all scans, at constant diffraction angles 26.5° and 40.2°; 46.5° which correspond to respectively the SpectroMembrane film and Pt foil, during discharge/charge process, the growing/disappearance of a series of new peaks, located at 8.2°, 16.4°, and 24.2° is observed. These peaks can be assigned to ZHS in agreement with previously reported experiments on both Mn-based[44–46] and vanadium-based[47–49] materials for rechargeable aqueous Zn-ion battery. The evolution of the intensity of these peaks confirms that upon discharge ZHS progressively precipitates (maximal intensity at 0.7 V vs Zn^{2+}/Zn) and, in a reversible way, is solubilized during the charge (no remaining diffraction peak above 1.6 V). The reversibility of this precipitation/dissolution process is confirmed as the same evolution is observed for subsequent discharge/charge cycles. The precipitation of such insulating ZHS on the cathode surface could also explain well the large resistance observed from EIS experiments during discharge below 1.4 V versus Zn^{2+}/Zn (Figure 4b). Another three peaks located at 10.5°, 15.3°, and 31.1° match well with $ZnSO_4·xH_2O$, that could be explained by the consummation of the water during ZHS formation. Peaks located at 12.5°, 36.7°, and 65.9° well match with KMO (the peak at 25.0° overlaps with the peak of the SpectroMembrane used to avoid electrolyte leakage from the cell), suggesting the good stability of the KMO structure and further confirms the effectiveness of pre-intercalation strategy. In addition, a slight shift of the (003) peak at 12.5° can be observed, suggesting ion (de)intercalation during the charge/discharge cycles. In summary, in situ XRD confirms the precipitation/dissolution process of ZHS in agreement with previous results,[45–49] but does not give clear evidence about intercalation of Zn^{2+} and/or proton in KMO. Therefore, an additional advanced characterization technique should be used to reveal the charge storage mechanism of aqueous Zn-ion batteries.

In the next step, EQCM has been used to study the charge storage mechanism of Mn oxide positive electrode during cycling in Zn-containing aqueous electrolyte. **Figure 6**a shows the CV profile at 5 mV s^{-1} of a KMO electrode in 2 M $ZnSO_4$ + 0.3 M $MnSO_4$ aqueous electrolyte. In these experiments, KMO powder was deposited onto the quartz resonator of an EQCM set-up, further used as the working electrode (see the experimental section for details). Two reduction peaks (1.4 V and 1.25 V vs Zn^{2+}/Zn) and one oxidation peak (1.62 V vs Zn^{2+}/Zn) can be observed during EQCM measurement, which is similar to the obtained previous results (Figure 4a). The validity of the gravimetric mode of EQCM measurements was checked by tracking the motional resistance change (ΔR) during the experiments. $\Delta F/\Delta R$ was found to be lower than 0.46% (see Figure 6b), thus validating the gravimetric mode and the further use of Sauerbrey's equation[50] to assign the change of the quartz resonance frequency in this potential range. Moreover, the average ΔR change from 0.8 to 1.75 V (oxidation) is close to zero; whereas from 1.75 to 0.8 V (reduction), a slight increase of the motional resistance (20 Ω) could be consistent with the formation of ZHS. This is in accordance with the large high-frequency loop showing up during reduction in Figure 4b. Figure 6c shows the CV of KMO at 10 mV s^{-1} (black line), and the blue lines correspond to the associated mass change measured by EQCM during the positive and the negative sweeps, calculated from Sauerbrey equation.[50] As noticed during the oxidation sweep, from 0.8 to 1.75 V versus Zn^{2+}/Zn (Figure 6c), the sharp oxidation peak of KMO is correlated with a drastic drop of the mass, in agreement with ion deintercalation from the structure (black line) together with, as highlighted by the in situ XRD study, the dissolution of ZHS. This is also consistent with a local increase of the motional resistance during the dissolution of the precipitate. But with an overall motional resistance over the whole oxidation sweep close to zero. Note that the weight increases during low anodic polarization (from 0.8 to 1.2 V vs Zn^{2+}/Zn) are likely due to the cathodic process still occurring upon potential reversal, up to about 1.2 V and could be also linked to the dissolution start of the ZHS, as observed from the slight increase of ΔR (Figure 6b). During the cathodic (reduction) sweep, from 1.75 to 0.8 V versus Zn^{2+}/Zn, ion intercalation into KMO and the precipitation of ZHS jointly result in an electrode mass increase—ΔR increase (Figure 6b) is likely correlated with the ZHS precipitation. Figure 6d shows the change of the electrode weight versus the charge passed in the electrode during the reduction process (from 1.75 to 0.8 V vs Zn^{2+}/Zn). Shaded areas represent the two potential regions where the

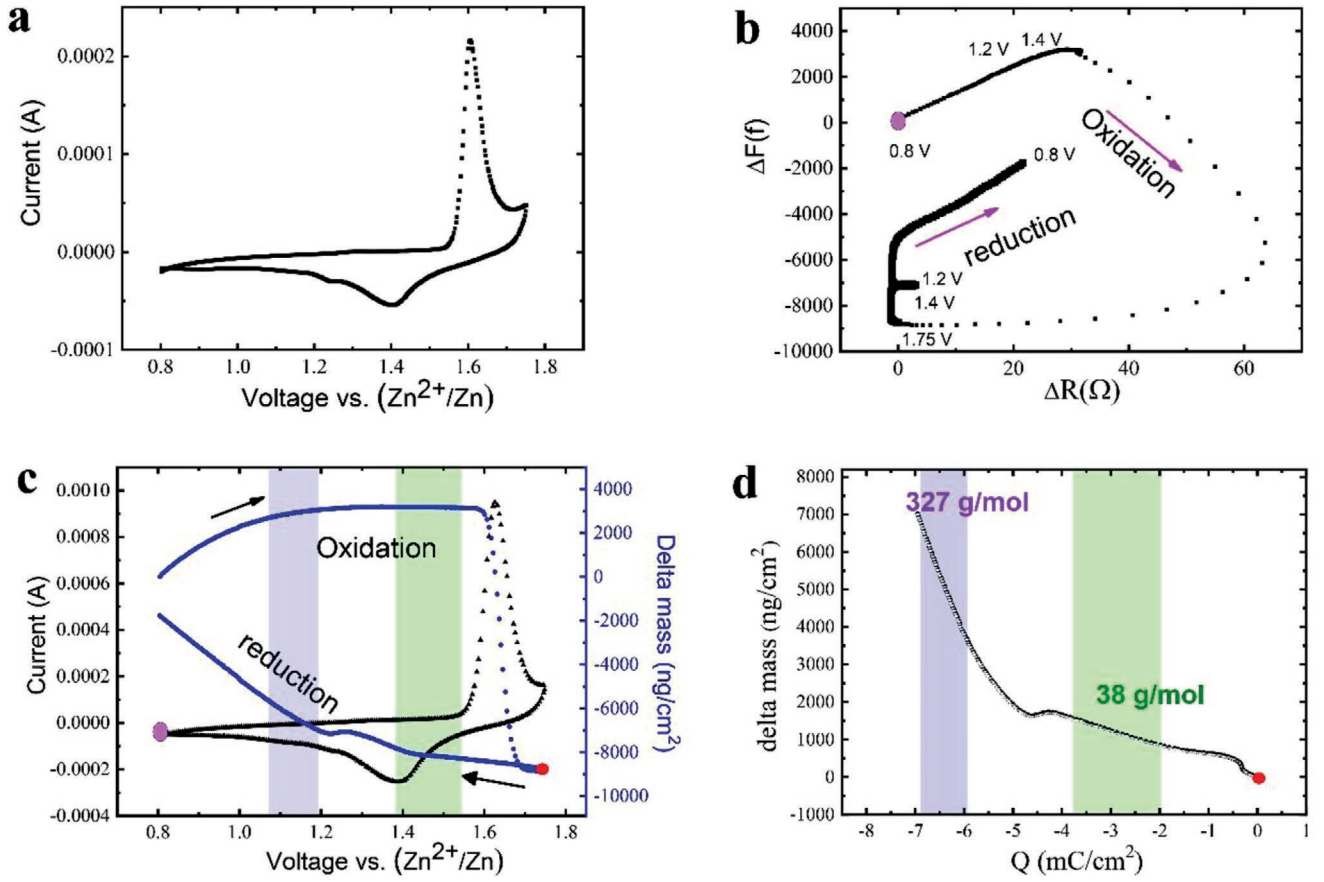

Figure 6. EQCM result of $K_{0.27}MnO_2{\cdot}0.54H_2O$ in 2 M $ZnSO_4$ + 0.3 M $MnSO_4$ electrolyte. a) CV test at 5 mv s^{-1}, b) Change of frequency versus motional resistance during the polarization at 10 mV s^{-1}. c) CV and EQCM frequency response at 10 mV s^{-1} and d) electrode mass change versus charge during the reduction polarization.

redox reactions occur as described in Figure 6c. Average molar weights of m/z = 38 $g{\cdot}mol^{-1}$ and 327 $g{\cdot}mol^{-1}$ were obtained in the high (around 1.4 V vs Zn^{2+}/Zn) and low (around 1.2 V vs Zn^{2+}/Zn) potential regions, respectively. As a result, the calculated heavy molar weight 327 $g{\cdot}mol^{-1}$ would support the precipitation of about 0.6 $Zn_4SO_4(OH)_6{\cdot}5H_2O$ (M_w=531 g mol^{-1}) ZHS molecules in the lower potential range (around 1.2 V vs Zn^{2+}/Zn), which well agrees with the previous in situ XRD result and the redox peak at 1.2 V as shown in Figure 4a, and with the ΔR increase observe in this region (Figure 6b). However, it is difficult to identify the cation responsible for charge compensation in the MnO_2 electrode, which could be Zn^{2+} or H^+. This is also the case during the first plateau at 1.4 V versus Zn^{2+}/Zn. Yet, a mechanism can be proposed in light of the precipitation of ZHS during the second plateau. Indeed, the intercalation of one H_3O^+ (M_w = 19 g mol^{-1}), together with H_2O molecule, seems consistent with the molar weight 38 g mol^{-1} observed in the high potential region (around 1.4 V vs Zn^{2+}/Zn). In this region, it can also be noticed the ΔR is zero (Figure 6b), which is expected for a pure intercalation mechanism. Also, and importantly, the H_3O^+ intercalation in the MnO_2 electrode would result in a local pH increase that could explain the precipitation of ZHS, leading to both a ΔR and a mass increase. A similar molar weight of 377 $g{\cdot}mol^{-1}$ was measured during the oxidation process (positive charge) as shown in Figure S9, Supporting Information, thus supporting the dissolution of ZHS and deintercalation of cations during the reverse process.

From the galvanostatic plots, 1F is exchanged during charge/discharge process. By combining in situ XRD and EQCM analysis, a reduction mechanism could be proposed (Equations (2)–(4)). The proposed equations are theoretical ones considering that each of the different processes are complete.

$$K_yMnO_2 + H_2O + e^- \rightarrow HK_yMnO_2 + OH^- \quad (2)$$

$$H_aK_bMnO_2 + H_2O \leftrightarrow \frac{1}{2}MnO_2 + \frac{1}{2}Mn^{2+} + aH^+ + bK^+ + 2OH^- \quad (a+b=1) \quad (3)$$

$$\frac{2}{3}Zn^{2+} + \frac{1}{6}SO_4^{2-} + xOH^- + \frac{5}{6}H_2O \rightarrow \frac{1}{6}ZnSO_4\,3Zn(OH)_2{\cdot}5H_2O\downarrow \quad (4)$$

The discharge is achieved by exchanging 1F, corresponding to the intercalation of 1 H^+ (Equation (2)). Although Zn^{2+} cation intercalation cannot be ruled out, it is unlikely to occur. The intercalation of H^+ (Equation (2)) leads to an increase of the local pH on the electrode surface and ZHS precipitation occurs according to Equation (4). Reverse process occurs during charge.

The reduction reaction starts at a potential of about 1.4 V versus Zn^{2+}/Zn, where protons intercalate into the KMO structure as a result of the reduction of Mn^{+IV} down to Mn^{+III} (Equation (2)) with a reversible capacity of 1F. The net mass increase of 38 $g.mol^{-1}$ obtained from EQCM measurements in this potential region (Figure 6d) is consistent with near-surface desolvation of H^+ ions from their water solvation, as previously observed by EQCM for Li intercalation in $LiFePO_4$ from aqueous electrolyte.[51] The resulting local pH increase at the electrode surface further leads to the precipitation of ZHS according to Equation (3)[44]—which leads to both a mass and ΔR increase, consistent with the formation of a precipitate, as shown in Figure 6b,c. The intercalation of H^+ cation in KMO well agrees with the local pH increase at the electrode surface for further ZHS precipitation, absence of important change in the interlayer distance of the KMO structure observed from in situ XRD measurements (Figure 5), and with faster diffusion of H^+ versus Zn^{2+}. As a result, although Zn^{2+} cation intercalation cannot be ruled out, it is unlikely to occur. Finally, the dismutation reaction of Mn^{+III} into soluble Mn^{2+} and Mn^{+IV} according to Equation (3) should occur. However, this reaction is strongly displaced to the left side ($H_aK_bMnO_2$ formation) thanks to the presence of Mn^{2+} via the addition of 0.1 M $MnSO_4$ in the electrolyte: only small amount of soluble Mn^{2+} is produced. This reaction can also be supported by the fact that protons and K^+ are in competition to occupy the same sites of MnO_2 to keep the structure stability in acidic electrolyte as reported by Ceder at al.[52] and Yin et al.[53] This well agrees with the reaction mechanism proposed by Pan et al.,[37] and it is also supported by the small weight loss observed by EQCM measurement in Figure 6c at 0.8 V versus Zn^{2+}/Zn, which is visible during three cycles (see Figure S10, Supporting Information). During the charging process, the reversible reactions occur to form back $H_aK_bMnO_2$,[40] leading to the decrease of pH value and ZHS dissolution. To get further insights into the mechanism, thermo gravimetric analysis (TGA) experiments were achieved on samples polarized at 1.2 and 1.4 V versus Zn^{2+}/Zn, after the second discharge. The DTG curve of KMO after cycling at 1.4 V versus Zn^{2+}/Zn (Figure S11a, Supporting Information) shows three small weight loss peaks at 207, 410, and 520 °C, similar to the TGA curve of MnO_2.[54] For the KMO after cycling at 1.2 V (Figure S11b, Supporting Information), weight loss peaks at 157, 267, and 397 °C are observed, in agreement with the different decomposition steps of ZHS into ZnO.[55]

Those results and the proposed mechanism are in good agreement with the work from Pan et al.[37] Moreover, results of the EQCM/in-operando XRD study provide the first direct evidence of the generation of ZHS during cycling, assumed to originated from the local pH increase as the consequence of proton intercalation.

3. Conclusions

A molten salt synthesis route was used to prepare 2D MnO_2 nanosheets pre-intercalated with alkali ions (Na^+, K^+), which was further used as electrode material for aqueous Zn-ion batteries. A $K_{0.27}MnO_2$ cathode could achieve a high capacity of 280 mAh g^{-1} at C/3, as well as, long cycling stability with 90% retention after 1000 cycles at 10C rate. These features firstly highlight the interest of the molten salt route for the preparation of nanomaterials with excellent performance for energy storage applications. Beyond that, we further combined EQCM together with in situ XRD techniques and thermogravimetric analysis to clarify the charge storage mechanism of KMO. Those measurements confirm the dissolution/precipitation mechanism of zinc hydrosulfate ZHS, as a result of the local pH increase following protons intercalation into the KMO structure. The results show the interest in the EQCM technique in gravimetric mode as an efficient tool to study complex charge storage mechanisms in the field of electrochemical energy storage.

4. Experimental Section

Preparation of 2D $K_{0.27}MnO_2{\cdot}0.54H_2O$ and $Na_{0.55}Mn_2O_4{\cdot}1.5H_2O$: In a typical procedure, 5 g of nitrate powder was placed into a quartz crucible and then transferred into the muffle furnace at a temperature of 350 °C (for $NaNO_3$) or 380 °C (for KNO_3) in the air atmosphere. Once the nitrate powder turns into the molten state after heating for ≈10 min, 0.2 g of $MnSO_4$ powder was added. After a short reaction time of 1 min, the sample was quenched in the air and washed with distilled water to remove excess nitrate powder.

Physical Characterizations: XRD data was collected using an X-ray diffractometer (X'Pert Pro, PANalytical). The morphology was analyzed by field-emission scanning electron microscopy (FEI Nova 450 Nano) and transmission electron microscopy with energy-dispersive X-ray spectroscopy (Tecnai G2 20 U-Twin and Titan G2 60-300). XPS (ESCALab 250) was used to determine the electronic state of the elements and to get information on the nature of compounds. TGA (Setaram TGDTA 92) was performed using an alumina crucible as sample holder, in Ar atmosphere with a ramping rate of 5 °C min^{-1}.

For the in-operando XRD test, 2-electrode Swagelok cells were assembled in air, using KMO as the working electrode deposited onto platinum disk as the current collector, and Zn metal disk as both counter electrode and reference electrodes. Before adding the KMO working electrode, a SpectroMembrane was placed onto the bottom part of the Swagelok cell to avoid electrolyte leakage. The in situ XRD cell was connected to a Biologic potentiostat to conduct the electrochemical cycling at a current rate of C/3. The XRD patterns were recorded in-operando during the galvanostatic test (a total of 5 min for one full pattern). AFM (Shimadzu) and high-resolution TEM were used to measure the thickness. Nitrogen adsorption desorption isotherms were measured at 77 K using a Micromeritics ASAP 2020.

Electrochemical Measurements: Rolled, free-standing KMO film electrodes were prepared with a specific composition (80 wt% of active material powders, 15 wt% of carbon black and 5 wt% of PTFE binder) and a controlled mass loading (around 2 mg cm^{-2}). Zinc metal foil was used as counter and reference electrode while a Pt disk served as a current collector for the KMO positive electrode (the electrochemical signature of KMO on six different current collectors have been compared in Figure S12, Supporting Information, while KMO on Pt disk and glass carbon have less polarization). Two layers of 260 µm-thick porous borosilicate glass fibers (Whatman GF/B) were used as a separator. The electrolyte was 2 M $ZnSO_4$ plus 0.3 M $MnSO_4$ (pH value is 3.8) since it is known that $MnSO_4$ leads to hampering the dissolution of Mn element, thus help to improve the cycling performance.[37] The electrolyte was purged with argon gas prior to use.

Cyclic voltammetry, EIS and galvanostatic cycling were performed using a VMP3 potentiostat (Biologic, France). Cyclic voltammetry and galvanostatic cycling were carried out within a potential range from 0.7 to 1.1 versus Zn^{2+}/Zn. EIS (EIS) was performed at open circuit potential with a 10 mV rms amplitude between from 200 kHz down to 10 mHz.

For sample preparation of the EQCM, Bio-Logic 1 in. diameter Au-coated quartz crystals (oscillating frequency, f_0, 5 MHz) were coated using a precise pipette (Gilson PIPET-MAN Classic P20) with a slurry

containing 80 wt% of active material KMO powder, 15wt% of conducting carbon (Super-P), and 5 wt% of polyvinylidene fluoride (Arkema, CAS #24937-79-9) binder in *N*-methyl-2-pyrrolidone (Sigma-Aldrich, CAS #872-50-4). The coated quartz crystal was placed on a PTFE holder in which the coated side was orientated toward the reference and the counter electrode served as the working electrode in a 3-electrode electrochemical cell. The reference electrode was a saturated calomel electrode and the electrolyte was 2 M $ZnSO_4$ together with 0.3 M $MnSO_4$. EQCM data were analyzed based on the Sauerbrey equation (Equation (5)):[50]

$$\Delta m = -C_f \times \Delta f \tag{5}$$

where Δm (g cm^{-2}) is the mass change of the coated quartz, C_f is sensitivity factor of the crystal (g cm^{-2} Hz^{-1}) and Δf is the quartz resonance frequency (Hz). The sensitivity factor of the coated quartz was obtained by performing a copper deposition experiment conducted in 0.1 M $CuSO_4$ mixed with 1 M H_2SO_4 by applying a constant current of 5 mA for 120 s. In this experiment, the C_f was calculated to be 12.3 ng·cm^{-2}·Hz^{-1} (taking into account the Au crystal electrode surface of 1.27 cm^2). For consistent results, few cycles were run before starting EQCM measurements, to obtain stable, reproducible electrochemical signatures. By giving a plot with the electrode weight change during polarization versus charge (Q), the molar weight of intercalated ions can be calculated according to Faraday's law in Equation (6):[50]

$$\frac{\Delta m}{\Delta Q} = \frac{M}{nF} \tag{6}$$

where ΔQ is the charge passed through the electrode in coulomb, M is the molar weight of the intercalated ions, F is the Faraday constant (96 485 C mol^{-1}), and n is the valence number of the ion.

Supporting Information

Supporting Information is available from the Wiley Online Library or from the author.

Acknowledgements

L.L. was supported by ERC Synergy Grant MoMa-Stor #951513. P.S. and P.-L.T. acknowledge the support from Agence Nationale de la Recherche (Labex Store-ex) and ERC Synergy Grant MoMa-Stor #951513. The authors acknowledge Sandrine Dulard and Barbara Daffos for their kind help in TEM and BET test.

Conflict of Interest

The authors declare no conflict of interest.

Data Availability Statement

Research data are available from corresponding author on reasonable request.

Keywords

alkali ions pre-intercalation, aqueous Zn-ion batteries, MnO_2, molten salt method

Received: April 23, 2021
Revised: May 28, 2021
Published online: June 26, 2021

[1] D. Kundu, S. H. Vajargah, L. Wan, B. Adams, D. Prendergast, L. F. Nazar, *Energy Environ. Sci.* **2018**, *11*, 881.
[2] H. Kim, J. Hong, K. Y. Park, H. Kim, S. W. Kim, K. Kang, *Chem. Rev.* **2014**, *114*, 11788.
[3] Y. Wang, J. Yi, Y. Xia, *Adv. Energy Mater.* **2012**, *2*, 830.
[4] D. Su, A. McDonagh, S.-Z. Qiao, G. Wang, *Adv. Mater.* **2017**, *29*, 1604007.
[5] N. Zhang, F. Cheng, J. Liu, L. Wang, X. Long, X. Liu, F. Li, J. Chen, *Nat. Commun.* **2017**, *8*, 405.
[6] B. W. Olbasa, F. W. Fenta, S. Chiu, C. Tsai, C. Huang, B. A. Jote, T. T. Beyene, F. Liao, C. Wang, W. Su, H. Dai, B. J. Hwang, **2020**, *3*, 4499.
[7] M. Song, H. Tan, D. Chao, H. J. Fan, *Adv. Funct. Mater.* **2018**, *28*, 1802564.
[8] C. Zhong, B. Liu, J. Ding, X. Liu, Y. Zhong, Y. Li, C. Sun, X. Han, Y. Deng, N. Zhao, W. Hu, *Nat. Energy* **2020**, *5*, 440.
[9] Q. Chen, J. Jin, Z. Kou, C. Liao, Z. Liu, L. Zhou, J. Wang, L. Mai, *Small* **2020**, *16*, 2000091.
[10] J. F. Parker, C. N. Chervin, I. R. Pala, M. Machler, M. F. Burz, J. W. Long, D. R. Rolison, **2017**, *418*, 415.
[11] C. Xu, B. Li, H. Du, F. Kang, *Angew. Chem.* **2012**, *124*, 957.
[12] T. Shoji, M. Hishinuma, T. Yamamoto, *J. Appl. Electrochem.* **1988**, *18*, 521.
[13] C. Wei, C. Xu, B. Li, H. Du, F. Kang, *J. Phys. Chem. Solids* **2012**, *73*, 1487.
[14] B. Lee, C. S. Yoon, H. R. Lee, K. Y. Chung, B. W. Cho, S. H. Oh, *Sci. Rep.* **2014**, *4*, 6066.
[15] M. H. Alfaruqi, J. Gim, S. Kim, J. Song, D. T. Pham, J. Jo, Z. Xiu, V. Mathew, J. Kim, *Electrochem. Commun.* **2015**, *60*, 121.
[16] T. Sun, Q. Nian, S. Zheng, J. Shi, Z. Tao, *Small* **2020**, *16*, 2000597.
[17] K. W. Nam, H. Kim, J. H. Choi, J. W. Choi, *Energy Environ. Sci.* **2019**, *12*, 1999.
[18] M. H. Alfaruqi, V. Mathew, J. Gim, S. Kim, J. Song, J. P. Baboo, S. H. Choi, J. Kim, *Chem. Mater.* **2015**, *27*, 3609.
[19] H. Zhang, Q. Liu, J. Wang, K. Chen, D. Xue, J. Liu, X. Lu, *J. Mater. Chem. A* **2019**, *7*, 22079.
[20] G. Fang, C. Zhu, M. Chen, J. Zhou, B. Tang, X. Cao, X. Zheng, A. Pan, S. Liang, *Adv. Funct. Mater.* **2019**, *29*, 1808375.
[21] J. Huang, Z. Wang, M. Hou, X. Dong, Y. Liu, Y. Wang, Y. Xia, *Nat. Commun.* **2018**, *9*, 2906.
[22] K. Chen, W. Pan, D. Xue, *J. Phys. Chem. C* **2016**, *120*, 20077.
[23] Y. Zhang, S. Deng, G. Pan, H. Zhang, B. Liu, X. L. Wang, X. Zheng, Q. Liu, X. Wang, X. Xia, J. Tu, *Small Methods* **2020**, *4*, 1900828.
[24] G. Liu, H. Huang, R. Bi, X. Xiao, T. Ma, L. Zhang, *J. Mater. Chem. A* **2019**, *7*, 20806.
[25] Q. Zhao, A. Song, S. Ding, R. Qin, Y. Cui, S. Li, F. Pan, *Adv. Mater.* **2020**, *32*, 2002450.
[26] X. Wen, C. He, B. Wu, X. Huang, Z. Huang, Z. Yin, Y. Liu, M. Fang, X. Wu, X. Min, *CrystEngComm* **2019**, *21*, 1809.
[27] T. Kimura, in *Advances in Ceramics—Synthesis and Characterization, Processing and Specific Applications*, (Ed: C. Sikalidis), IntechOpen, London **2011**.
[28] Z. Hu, X. Xiao, H. Jin, T. Li, M. Chen, Z. Liang, Z. Guo, J. Li, J. Wan, L. Huang, Y. Zhang, G. Feng, J. Zhou, *Nat. Commun.* **2017**, *8*, 15630.
[29] L. Liu, Y.-C. Wu, P. Rozier, P.-L. Taberna, P. Simon, *Research* **2019**, *2019*, 6585686.
[30] A. Monshi, M. R. Foroughi, M. R. Monshi, *World J. Nano Sci. Eng.* **2012**, *2*, 154.
[31] W. Sun, F. Wang, S. Hou, C. Yang, X. Fan, Z. Ma, T. Gao, F. Han, R. Hu, M. Zhu, C. Wang, *J. Am. Chem. Soc.* **2017**, *139*, 9775.
[32] D. Chao, W. Zhou, C. Ye, Q. Zhang, Y. Chen, L. Gu, K. Davey, S. Z. Qiao, *Angew. Chem., Int. Ed.* **2019**, *58*, 7823.
[33] S. Islam, M. H. Alfaruqi, V. Mathew, J. Song, S. Kim, S. Kim, J. Jo, J. P. Baboo, D. T. Pham, D. Y. Putro, Y. K. Sun, J. Kim, *J. Mater. Chem. A* **2017**, *5*, 23299.

[34] H. Ren, J. Zhao, L. Yang, Q. Liang, S. Madhavi, Q. Yan, *Nano Res.* **2019**, *12*, 1347.
[35] L. Liu, Z. Lin, J. Y. Chane-Ching, H. Shao, P. L. Taberna, P. Simon, *Energy Storage Mater.* **2019**, *19*, 306.
[36] C. Xu, B. Li, H. Du, F. Kang, *Angew. Chem., Int. Ed.* **2012**, *51*, 933.
[37] H. Pan, Y. Shao, P. Yan, Y. Cheng, K. S. Han, Z. Nie, C. Wang, J. Yang, X. Li, P. Bhattacharya, K. T. Mueller, J. Liu, *Nat. Energy* **2016**, *1*, 16039.
[38] S. D. Han, S. Kim, D. Li, V. Petkov, H. D. Yoo, P. J. Phillips, H. Wang, J. J. Kim, K. L. More, B. Key, R. F. Klie, J. Cabana, V. R. Stamenkovic, T. T. Fister, N. M. Markovic, A. K. Burrell, S. Tepavcevic, J. T. Vaughey, *Chem. Mater.* **2017**, *29*, 4874.
[39] Y. Jin, L. Zou, L. Liu, M. H. Engelhard, R. L. Patel, Z. Nie, K. S. Han, Y. Shao, C. Wang, J. Zhu, H. Pan, J. Liu, *Adv. Mater.* **2019**, *31*, 1900567.
[40] X. Guo, J. Zhou, C. Bai, X. Li, G. Fang, *Mater. Today Energy* **2020**, *16*, 100396.
[41] S. H. Kim, S. M. Oh, *J. Power Sources* **1998**, *72*, 150.
[42] A. J. Bard, L. R. Faulkner, *Electrochemical Methods: Fundamentals and Applications*, 2nd ed., John Willey & Sons Inc., New York **2001**.
[43] A. R. C. Bredar, A. L. Chown, A. R. Burton, B. H. Farnum, *ACS Appl. Energy Mater.* **2020**, *3*, 66.
[44] B. Lee, H. R. Seo, H. R. Lee, C. S. Yoon, J. H. Kim, K. Y. Chung, B. W. Cho, S. H. Oh, *ChemSusChem* **2016**, *9*, 2948.
[45] C. Zhu, G. Fang, J. Zhou, J. Guo, Z. Wang, C. Wang, J. Li, Y. Tang, S. Liang, *J. Mater. Chem. A* **2018**, *6*, 9677.
[46] V. Soundharrajan, B. Sambandam, S. Kim, V. Mathew, J. Jo, S. Kim, J. Lee, S. Islam, K. Kim, Y. K. Sun, J. Kim, *ACS Energy Lett.* **2018**, *3*, 1998.
[47] C. Liu, Z. Neale, J. Zheng, X. Jia, J. Huang, M. Yan, M. Tian, M. Wang, J. Yang, G. Cao, *Energy Environ. Sci.* **2019**, *12*, 2273.
[48] P. Hu, T. Zhu, X. Wang, X. Wei, M. Yan, J. Li, W. Luo, W. Yang, W. Zhang, L. Zhou, Z. Zhou, L. Mai, *Nano Lett.* **2018**, *18*, 1758.
[49] F. Wan, L. Zhang, X. Dai, X. Wang, Z. Niu, J. Chen, *Nat. Commun.* **2018**, *9*, 1656.
[50] G. Sauerbrey, *Z. Phys.* **1959**, *155*, 206.
[51] P. Lemaire, T. Dargon, D. A. D. Corte, O. Sel, H. Perrot, J. M. Tarascon, *Anal. Chem.* **2020**, *92*, 13803.
[52] D. A. Kitchaev, S. T. Dacek, W. Sun, G. Ceder, *J. Am. Chem. Soc.* **2017**, *139*, 2672.
[53] B. Yin, S. Zhang, H. Jiang, F. Qu, X. Wu, *J. Mater. Chem. A* **2015**, *3*, 5722.
[54] J. Zia, E. S. Aazam, U. Riaz, *J. Mater. Res. Technol.* **2020**, *9*, 9709.
[55] T. Staminirova, N. Petrova, G. Kirov, *J. Therm. Anal. Calorim.* **2016**, *125*, 85.